ELSEVIER

Polymer 42 (2001) 5829–5839

polymer

www.elsevier.nl/locate/polymer

Phase structures and morphologies determined by self-organization, vitrification, and crystallization: confined crystallization in an ordered lamellar phase of PEO-*b*-PS diblock copolymer

L. Zhu[a], S.Z.D. Cheng[a,*], B.H. Calhoun[a], Q. Ge[a], R.P. Quirk[a], E.L. Thomas[b], B.S. Hsiao[c], F. Yeh[c], B. Lotz[d]

[a]*The Maurice Morton Institute and Department of Polymer Science, The University of Akron, 170 University Circle, Akron, OH 44325-3909, USA*
[b]*Department of Materials Science and Engineering, Massachusetts Institute and Technology, Cambridge, MA 02139, USA*
[c]*Department of Chemistry, The State University of New York at Stony Brook, Stony Brook, NY 11794-3400, USA*
[d]*Institute Charles Sadron, 6 Rue Boussingault, Strasbourg 67083, France*

Received 7 March 2000; received in revised form 1 December 2000; accepted 6 December 2000

Abstract

Phase morphology, crystal orientation, and overall crystallization kinetics as determined by self-organization of the diblock copolymer, vitrification of the amorphous block, and crystallization of the crystallizable blocks have been investigated for a lamellar-forming poly(ethylene oxide)-*b*-polystyrene (PEO-*b*-PS) diblock copolymer. The diblock copolymer has number-average molecular weights of 8700 g/mol for the PEO blocks and 9200 g/mol for the PS blocks. Based on wide angle X-ray diffraction (WAXD) observations, the PEO crystals possess the same crystal structure as pure PEO. When the crystallization temperature (T_c) is below 40°C, the PEO crystals melt below 55°C, which is much lower than the melting point of their homopolymer analogs. The glass transition temperature of the PS blocks is 62°C, determined by the 50% heat capacity change during vitrification observed in differential scanning calorimetry (DSC). The order–disorder transition temperature is determined to be 160°C using a one-dimensional (1D) small angle X-ray scattering (SAXS) experiment. The mean-field segmental interaction parameter is determined to be $\chi_{EO/St} = -7.05 \times 10^{-3} + 21.3/T$, based on the SAXS scattering intensity analysis for $T > T_{MF}$ (crossover temperature from the concentration-fluctuation region to the mean-field region). Using real-time resolved simultaneous SAXS and WAXD techniques, the PEO block is observed to crystallize within the confined lamellae provided by the glassy PS layers. The crystal (the $\hat{c}-$ axis) orientation within the confined lamellae is determined by combined two-dimensional (2D) SAXS and WAXD experiments. The PEO crystals are observed to tilt away from the lamellar surface normal ($\hat{n}$) at $T_c <$ 35°C, while they are oriented parallel to $\hat{n}$ when crystallized above 35°C. The thickness changes in the lamellar phase morphology after isothermal crystallization can also be observed when compared with that in the molten state using 1D SAXS. After the crystallization of PEO blocks, the phase lamellar thickness slightly decreases with decreasing T_c when $T_c < 35$°C. When $T_c > 35$°C, the lamellar thickness slightly increases with increasing T_c. At $T_c = 35$°C, the thickness remains identical to that in the molten state. The increase of phase lamellar thickness may be a result of both dimensional change of the crystal growth via thickening of PEO lamellar crystals, and weakening of the confinement of the PS glass layers. The isothermal crystallization kinetics and melting results observed in DSC also support these conclusions. © 2001 Elsevier Science Ltd. All rights reserved.

Keywords: Crystalline–amorphous diblock copolymers; Confined crystallization; Crystal orientation

1. Introduction

Block copolymers are of great scientific interest due to their self-assembled supra-molecular structures formed under various conditions [1,2]. In diblock copolymers, the well-known phase morphologies include lamellae, double gyroids, cylinders, and spheres. In the weak segregation limit, order-to-order and order-to-disorder transitions are of most interest. Many ordered phases have also been observed in ABC type block copolymers [3]. Besides amorphous–amorphous diblock copolymers, liquid crystalline–amorphous diblock copolymers and semicrystalline–amorphous diblock copolymers have obtained substantial attention, because molecular and supra-molecular self-assemblies can form at different length scales [4]. For

* Corresponding author. Tel.: +1-330-972-6931; fax: +1-330-972-8626.
E-mail address: cheng@polymer.uakron.edu (S.Z.D. Cheng).

0032-3861/01/$ - see front matter © 2001 Elsevier Science Ltd. All rights reserved.
PII: S0032-3861(00)00902-2

example, micro-phase separation of the diblock copolymers usually occurs on a scale of a few tens of nm, layers of low ordered liquid–crystalline phases formed by the liquid crystalline blocks are usually on a scale of a few nm, and crystallization of the crystalline blocks is on an atomic packing scheme of a few tenths of nm.

In crystalline–amorphous diblock copolymer systems, there are three factors that determine the final phase and crystalline morphology of these diblock copolymers, i.e. the microphase separation of a diblock copolymer (the order–disorder transition temperature, T_{ODT}), the crystallization of the crystallizable blocks (the crystallization temperature, T_c), and the vitrification of the amorphous blocks (the glass transition temperature, T_g^a). Therefore, competitions among these three processes can be understood by the relative positions of these three temperatures [5]. In disordered and weakly segregated low molecular weight crystalline–amorphous diblock copolymers, when the $T_g^a \ll T_{ODT}$ and T_c, and the viscosity of the system is relatively low, unconfined crystallization takes place, because this process possesses much stronger molecular interaction compared to microphase separation. The crystallization thus overwrites the existing phase morphology to form a crystalline lamellar morphology, and memory of the initial phase morphology is lost. When the $T_{ODT} < T_c$, unconfined crystallization occurs from a disordered phase as in the case of $T_c > T_{ODT} \gg T_g^a$ [5–8], while when the $T_{ODT} > T_c \gg T_g^a$, unconfined crystallization takes place from an ordered phase [7–16].

If the $T_g^a > T_c$, crystallization becomes confined and the existing phase morphology exerts strong restrictions on crystallization of the crystallizable blocks. As a consequence, the existing phase morphology is preserved after crystallization. Confined crystallization has been observed in both disordered and ordered phases, depending upon the T_{ODT}. When $T_g^a > T_c$ and T_{ODT}, the crystallization is confined in a concentration-fluctuation-induced disordered phase [5]. If $T_{ODT} > T_g^a > T_c$, the crystallization is confined within the existing ordered phase due to the rapid vitrification of the amorphous phases [17–26]. Although in some cases T_c is higher than T_g^a, partially confined crystallization may also occur in strongly segregated crystalline–amorphous diblock copolymers [27–29], in which the T_{ODT} is much higher than the T_c and T_g^a. This may be due to a strong microphase separation between the two immiscible blocks, and only local segmental rearrangements occur when relatively rapid crystallization takes place.

Understanding crystal orientation under confined crystallization conditions is also of interest. Generally speaking, there are two extremes of chain orientations in polymer crystals associated with microphase-separated nano-lamellae, i.e. the chain direction (usually the $\hat{c}$ − axis of the crystal) is oriented either parallel [6,30–33] or perpendicular [18–21,34] to the lamellar surface normal ($\hat{n}$). In a few cases, tilted chain orientation in the crystals with respect to $\hat{n}$ was also inferred from experimental results [11,35,36]. The origin of different chain orientations was speculated to relate to different molecular weights of the crystallizable blocks [11]. The perpendicular crystal orientation with respect to $\hat{n}$ was also speculated to be facilitated by the intermaterial dividing surface of the block copolymers [19].

In this work, confined crystallization behaviors in the case of $T_{ODT} > T_g^a > T_c$ is studied in an ordered lamellar PEO-*b*-PS diblock copolymer with relatively low molecular weights (8.7–9.2 k). Using time-resolved simultaneous small angle X-ray scattering (SAXS) and wide angle X-ray diffraction (WAXD) on the study of the crystallization process and subsequent crystal melting, crystals of the PEO blocks are observed to be constrained in the confined lamellar environment. It is also found by two-dimensional (2D) SAXS and WAXD that the PEO crystal (the $\hat{c}$-axis) orientation between two PS layers changes from inclined to parallel to $\hat{n}$ as the T_c increases from 15 to 40°C. As soon as the confinement is slightly weakened (i.e. the PS phase is slightly devitrified), the release of this constraint for the PEO crystals can be identified.

2. Experimental section

2.1. Materials and sample preparation

The PEO-*b*-PS diblock copolymer was synthesized *via* sequential anionic polymerization. The detailed procedure can be found elsewhere [37]. Polymerization of styrene (4 g, 38.5 mmol) in benzene was effective at room temperature using *sec*-BuLi (0.28 ml, 0.42 mmol) as the initiator in vacuum sealed glass reactors using breakseals and standard high-vacuum techniques [38]. After 24 h, an aliquot of poly(styryl)lithium was removed from the reactor and terminated with degassed methanol for sampling. The living poly(styryl)lithium (2 g, 0.217 mmol) remaining in the reactor was end-capped with ethylene oxide (9-fold excess, 0.11 ml, 2.17 mmol) by smashing the corresponding breakseal. The reaction was stirred at room temperature for 24 h and then 1.2 eq. of *tert*-butyl polyiminophosphazene (0.26 ml, 0.26 mmol) was added, followed by further addition of ethylene oxide (2.14 g, 48.6 mmol) to continue the block copolymerization at 45°C. The reaction was completed after 3 days and terminated with acidic methanol. The product was precipitated into hexane with quantitative yield. The crude polymer contained a small amount of PEO homopolymer, which was removed by column chromatography on microcrystalline cellulose using methanol as eluent solvent. The PS precursor was characterized by size exclusion chromatography (SEC) using polystyrene standard calibration, and had an $\bar{M}_n$ of 9.2 k and a polydispersity of 1.02. The $\bar{M}_n$ of the PEO block was determined by proton nuclear magnetic resonance (^{1}H NMR) to be 8.7 k, and the polydispersity of 1.04 in the final diblock copolymer was determined by SEC using universal calibration. The mass

Table 1
Densities and electron densities of amorphous PS and amorphous PEO, and volume fraction of PEO blocks at different temperatures (The calculations are based on the equation provided in Ref. [39])

Temperature (°C)	ρ_{PEO} (g/cm^3)	ρ_{PS} (g/cm^3)	ρ_e^{PEO} (e/nm^3)	ρ_e^{PEO} (e/nm^3)	f_{PEO} (%)
20	1.1210	1.0534	368	341	47.1
40	1.1067	1.0443	363	339	47.2
60	1.0919	1.0351	359	336	47.3
80	1.0767	1.0256	354	332	47.4
100	1.0610	1.0159	348	329	47.5
120	1.0446	1.0060	343	326	47.7
140	1.0277	0.9958	337	323	47.8
160	1.0101	0.9854	332	319	48.0
180	0.9917	0.9748	326	316	48.2
200	0.9725	0.9639	319	312	48.4
220	0.9524	0.9526	313	309	48.6

and electron densities of amorphous PS and PEO at different temperatures are listed in Table 1, based on the calculations by McGowan [39]. The volume fraction of PEO blocks (f_{PEO}) is thus 0.473 in the melt at 60°C.

In order to ensure the consistency of the phase behavior, uniform sample preparation procedure and thermal history were necessary. The sample was cast from a 5% (w/v) toluene solution, and the solvent was allowed to evaporate slowly under a dry nitrogen atmosphere at 50°C to prevent the crystallization of the PEO block. Residual solvent was removed under vacuum at 50°C for 1 day, and the sample was then annealed at 95°C for 12 h. The samples were studied using different experimental techniques including time-resolved simultaneous synchrotron SAXS and WAXD, and differential scanning calorimetry (DSC). In order to study the crystal orientation in this copolymer, the microphase separated samples were subjected to a large-amplitude oscillating shear at 110°C to achieve a uniform, parallel alignment of the lamellar phase morphology. The shear frequency was 0.5 Hz, and the shear amplitude was 150%. The shear-aligned samples were further annealed at 95°C for another 12 h in vacuum to eliminate any residual stresses.

2.2. Equipment and experiments

Time-resolved, simultaneous SAXS and WAXD experiments were conducted at the synchrotron X-ray beamline X27C of the National Synchrotron Light Source in Brookhaven National Laboratory. The wavelength of the X-ray beam was 0.1307 nm. One-dimensional (1D) position sensitive detectors (PSDs) were used to record the X-ray scattering. The zero pixel of the SAXS PSD was calibrated with a rat tail, and the scattering vector q ($q = 4\pi \sin\theta/\lambda$, where $\lambda = 0.1307$ nm and 2θ is the scattering angle) was calibrated with silver behenate. The WAXD PSD was calibrated using α-Al_2O_3. In addition, conventional SAXS was performed in some cases on an 18 kW rotating anode and 1D PSD using a combined slit and pinhole collimation system. For the oriented samples, 2D SAXS experiments were also carried out at the X27C synchrotron beamline using image plates as detectors. The corresponding WAXD experiments were conducted on the rotating anode generator equipped with a 2D image plate. The same samples were used in both the SAXS and WAXD experiments. The calibrations of conventional SAXS and WAXD in our laboratory were the same as in the synchrotron X-ray experiments.

Isothermal crystallization measurements were carried out on a customized two-chamber hot stage. The isothermal crystallization temperature (T_c) was controlled to within ±0.1°C. The samples were preheated to 70°C in the melting chamber for 3 min, and then quenched (switched) to the second chamber with preset temperatures for isothermal crystallization. A heating rate of 1°C/min was used to study the melting behavior of the samples after complete crystallization. In order to detect the T_{ODT} of the sample, SAXS experiments were also conducted up to 230°C at a heating rate of 2°C/min under a dry nitrogen atmosphere. The PEO-*b*-PS diblock copolymer is stable up to 250°C under an inert gas atmosphere for 3 h, as evidenced by combined thermogravimetric analysis and SEC results.

DSC experiments were carried out on a TA-2000 DSC to study the isothermal crystallization and melting behavior of the PEO-*b*-PS. The DSC was calibrated with *p*-nitrotoluene, naphthalene, and indium standards. Isothermal crystallization was conducted by quenching the samples from the melt at 70°C to a preset T_c. The fully crystallized samples were then heated at a rate of 5°C/min. The endothermic peak temperature was taken as the melting temperature (T_m). The weight percentage crystallinity was calculated using an equilibrium heat of fusion for low molecular weight PEO crystals (7.89 kJ/mol) [40].

Transmission electron microscopy (TEM, JEOL 1200 EX II) experiments were carried out at an accelerating voltage of 120 kV. Thin slices for TEM were obtained using a Reichert Ultracut S (Leica) microtome to section the shear-aligned samples perpendicular to the shear direction at −40°C. The sample was stained using RuO_4 vapor at room temperature for 20 min [41].

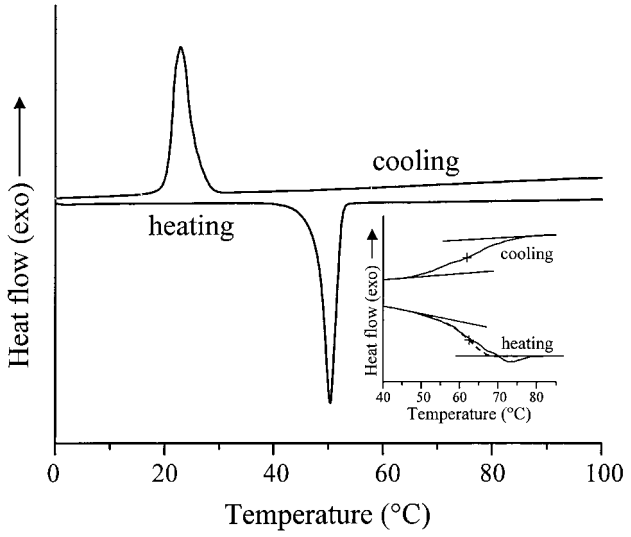

Fig. 1. DSC cooling and successive heating diagrams of the PEO-*b*-PS (8.7–9.2 k) at a rate of 5°C/min. The insert represents the glass transition region of the copolymer with an enlarged heat flow scale (× 17).

3. Results and discussion

3.1. General characterization of the diblock copolymer

Fig. 1 shows a set of DSC cooling and subsequent heating diagrams for the PEO-*b*-PS (8.7–9.2 k) at 5°C/min. On cooling, a major exothermic T_c peak occurs at about 26°C, and upon heating, an endothermic T_m peak appears at about 50°C. An inset of Fig. 1, which is seventeen-time magnified in the heat-flow scale, shows that a T_g^{PS} is located at 62°C upon cooling, determined by the 50% heat capacity (c_p) change during vitrification. During heating, the difference in the onset temperature (45°C), where the c_p deviates from the solid state c_p, and the ending temperature (77°C), where the c_p merges, is 32°C. The breadth of the T_g is significantly wider than the base polystyrene (about 18°C). Furthermore, the T_g of the base PS homopolymer is 85°C, which is 23°C higher than the T_g^{PS}. Both the lower T_g^{PS} and the wider T_g range may be the result of size and interface effects of the PS glass layers being located between molten PEO layers.

Fig. 2 shows a TEM micrograph of a thin section of this PEO-*b*-PS stained by RuO_4 at room temperature for 20 min. The geometry of the shear-aligned sample is defined by $\hat{x}$, $\hat{y}$, and $\hat{z}$ coordinates. The shear direction is along $\hat{x}$, and the shear plane is the $\hat{x}$–$\hat{y}$ plane. Thus, $\hat{z} \equiv \hat{n}$. In Fig. 2, layer morphology can be clearly observed perpendicular to the shear direction. Since PEO is more reductive than PS, it is more ready to be stained by RuO_4. The darker lines in the micrograph are the PEO layers, and the lighter lines are the PS layers. The boundary between two phases appears to be rough, because RuO_4 stains both PEO and PS phases. The short time staining procedure used may cause non-uniformity during staining. Therefore, create the roughness of the phase boundaries. The results of SAXS at 55°C in Fig. 3 also reveal the well-ordered lamellar phase morphology in the melt. The SAXS Bragg scattering peaks possess ratios of $q/q^* = 1 : 2 : 3 : 4$ (q^* is the scattering vector of the first-order peak). The first-order scattering peak corresponds to a Bragg spacing of 18.7 nm ($2\pi/q^*$). Therefore, from TEM and SAXS observations, the thicknesses of the PEO and PS layers can be calculated to be between 8.8 and 9.9 nm, respectively, based on the volume fraction of PEO blocks. The intensity of the second-order scattering peak is weaker than that of the third-order peak (Fig. 3). This may be explained by the extinction rule of structural symmetry. In the melt, the sample is in a two-phase system. The volume fraction of PEO blocks is close to 0.5, and thus, both of the PEO and PS layers are of similar thickness. This leads to a weak second-order scattering.

The order–disorder transition temperature (T_{ODT}) of this sample can be studied using temperature dependent SAXS. An inset of Fig. 4 shows a set of 1D SAXS patterns starting at 107°C, well above the T_m of the PEO crystals. Only the first order scattering peak is observed, because the electron density difference between amorphous PEO and PS further decreases at high temperatures (see Table 1). With increasing temperature, the first-order scattering peak shows a slight shift of the peak position towards higher q values.

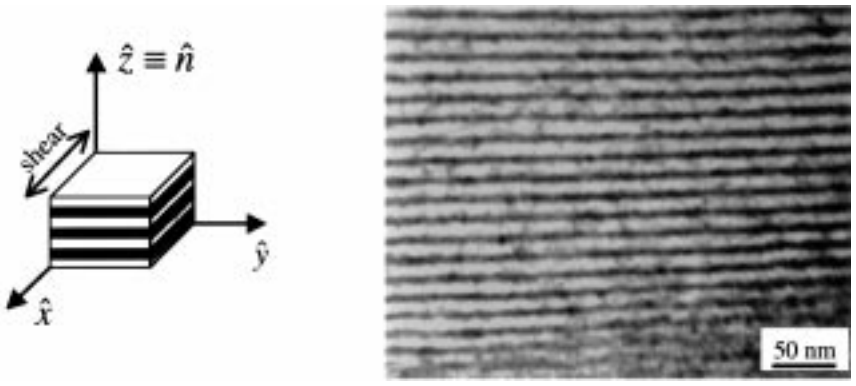

Fig. 2. TEM observation of the lamellar phase morphology of the PEO-*b*-PS after staining using RuO_4. The shear direction is along $\hat{x}$, and the shear plane is the $\hat{x}$–$\hat{y}$ plane. The lamellar geometry is defined as $\hat{n} \parallel \hat{z}$.

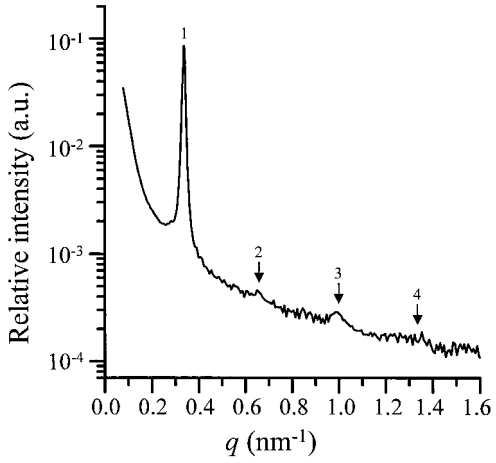

Fig. 3. A SAXS curve for the PEO-*b*-PS diblock copolymer obtained at 55°C. Note the second and third order scattering maxims.

The scattering intensity of the peak gradually decreases accompanied by a widening of the half-width at half-maximum (HWHM). At 160°C, there is a sudden decrease in the scattering intensity accompanied by a significant broadening in the HWHM, indicating the transition from the ordered lamellae to a disordered state. With further increase in the temperature, the broad scattering peak (correlation hole scattering) continuously shifts to higher q values, and its intensity decreases while the HWHM continues to increase. In order to clearly determine this transition, a relationship between the reciprocal maximum intensity (I_m^{-1}) and reciprocal temperature (T^{-1}) is plotted in Fig. 4. A discontinuous change of the reciprocal intensity at 160°C can be observed. The square of the HWHM (σ_q) with respect to T^{-1} is also included in this figure, and a similar relationship can be found as in the case of I_m^{-1} vs. T^{-1}. Both results indicate that the T_{ODT} is at 160°C. As shown in Fig. 4, above 160°C, a non-linear relationship between I_m^{-1} and T^{-1} reveals that the disordered state can be described by the concentration fluctuation theory [42], where both the PEO-rich and PS-rich microdomains possess the sinusoidal-wave-type profile interfaces [43,44]. Above ~200°C, the linear relationship between the I_m^{-1} and T^{-1} indicates that the disordered system can be described by the mean-field theory [45]. This crossover temperature is denoted as T_{MF}.

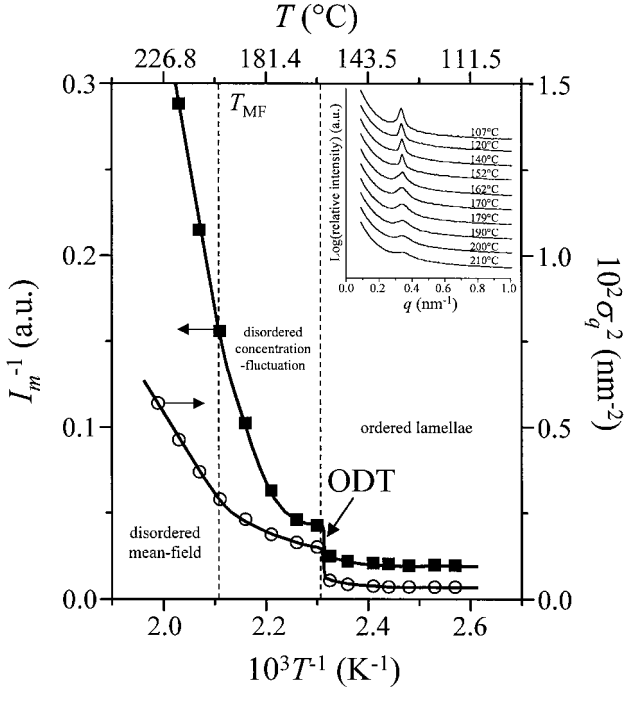

Fig. 4. Plots of the reciprocal X-ray scattering intensity (I^{-1}) and square of half width at half-height (σ_q) with respect to reciprocal temperature (T^{-1}) for the SAXS data of PEO-*b*-PS (8.7–9.2 k) obtained at different temperatures. The insert shows a set of SAXS data in a plot between relative intensity and scattering vector (q).

The Flory–Huggins segmental interaction parameter for the PEO-*b*-PS diblock copolymer ($\chi_{EO/St}$) can be estimated by analyzing the scattering profiles from the disordered melts on the basis of Leibler's Landau type mean-field theory [45] modified for the effects of molecular weight polydispersity and asymmetry in the segmental volume. The detailed theoretical calculations can refer to the work in Ref. [46]. For the estimation of $\chi_{EO/St}$ the characteristic parameters for this diblock copolymer are listed in Table 2. The molecular volume for styrene (v_{St}) and ethylene oxide (v_{EO}) are estimated as

$$v_{St} = M_{St}/\rho_{St} \quad (1)$$

and

$$v_{EO} = M_{EO}/\rho_{EO} \quad (2)$$

where M_{St} and M_{EO} are the molecular weights of styrene and ethylene oxide monomers. ρ_{St} and ρ_{EO} are the densities of amorphous PS and PEO, and are listed in Table 1. The segmental lengths for PEO (b_{EO}) and PS (b_{St}) are set as floating parameters to fit the experimental and theoretical peak scattering vector q_m. The initial values are taken as $b_{EO} = 0.50$ nm and $b_{St} = 0.68$ nm, respectively, calculated from the unperturbed molecular dimensions of linear PEO and PS chains [47]. The $\chi_{EO/St}$ results obtained from the best fit between the experimental and theoretical relative

Table 2
Characteristic parameters for the evaluation of the Flory–Huggins interaction parameter for this PEO-*b*-PS diblock copolymer ($\chi_{EO/St}$)

w_{EO} [a]	$N_{EO,n}$ [b]	$N_{St,n}$ [b]	λ [c]	$r_{c,n}$ [d]
0.486	198	88	1.08	264

[a] Weight fraction of the PEO blocks.
[b] $N_{EO,n}$ and $N_{St,n}$ are number-average degrees of polymerization of PEO and PS blocks.
[c] λ is a term for the molecular weight distribution correction. We assume $\lambda_{PEO} = \lambda_{PS} = \lambda_{PEO-b-PS} = [(M_w/M_n - 1)/(w_{EO}^2 + w_{St}^2)] + 1$.
[d] $r_{c,n}$ is the effective degree of polymerization, which has been corrected for the asymmetry in the segment sizes for PEO and PS, and $r_{c,n} = (v_{EO}/v_0)N_{EO,n} + (v_{St}/v_0)N_{St,n}$. v_0 is the reference volume, and $v_0 = (v_{EO}v_{St})1/2$.

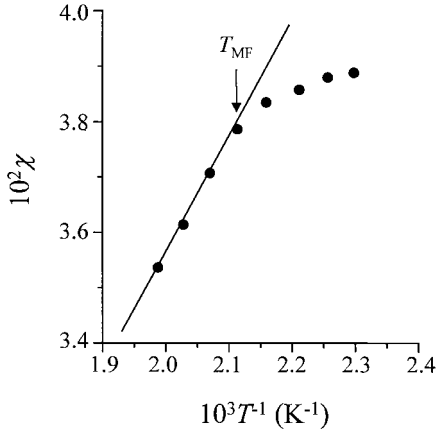

Fig. 5. $\chi_{EO/St}$ dependence on T^{-1}. From the linear region, the relationship of $\chi_{EO/St} = A + B/T$ can be obtained.

scattering intensity distributions are shown in Fig. 5 as a function of T^{-1}. In this plot, there also exists a T_{MF} around 200°C. At $T > T_{MF}$, $\chi_{EO/St}$ increases linearly with T^{-1}, but it tends to level off at $T < T_{MF}$. The plateau behavior can be explained by the thermal fluctuation effect in a real system, which tends to make the amplitude of the concentration fluctuations smaller than that predicted by the mean-field theory. Based on this theory, the linear part of $\chi_{EO/St}$ vs. T^{-1} at $T > T_{MF}$ can be expressed as

$$\chi_{EO/St} = -7.05 \times 10^{-3} + 21.3/T \qquad (T \text{ in K}) \tag{3}$$

The $(\chi_{EO/St} r_{c,n})_{ODT}$ calculated from Eq. (3) is 11.1 (T_{ODT} = 433 K), which is slightly higher than the critical value of $(\chi_{EO/St} r_{c,n})_c = 10.5$ predicted by mean-field theory for symmetric diblock copolymer. Here, $r_{c,n}$ is the effective degree of polymerization for the diblock copolymer, which has been corrected for the asymmetry in the segment sizes of PEO and PS (see Table 2). The higher $(\chi_{EO/St} r_{c,n})_{ODT}$ value compared to 10.5 indicates the "finite size effect" in the concentration fluctuation region [42]. This result is reasonable because the volume fraction of this diblock copolymer is close to 0.5, and it is near the critical point in the diblock copolymer phase diagram. The $\chi_{EO/St}$ value obtained for this diblock copolymer in the temperature range studied (160–230°C) changes from 0.035 to 0.039, which is smaller than those reported in the literature for the bulk $\chi_{EO/St}$ [48–50].

3.2. Confined PEO crystallization within lamellar morphology

Fig. 6a and b show sets of time-resolved, simultaneous synchrotron 1D SAXS and WAXD results for an unoriented PEO-*b*-PS sample crystallized at 35°C. The small angle scattering intensity in the melt is observed to be lower than that after crystallization of the PEO blocks, because the electron densities decrease in the order of crystalline PEO, amorphous PEO, and amorphous PS (407, 368, and 341 e/nm^3). Here, the density of crystalline PEO is 1.239 g/cm^3 [51]. In the initial stage (within 1.5 min) the SAXS patterns always have a sharp scattering peak from the ordered microphase separated lamellae in the melt, and the WAXD patterns show an amorphous halo arising from non-crystalline PEO and PS blocks. With increasing isothermal time (t_c), the intensity of the first-order scattering peak in the SAXS increases, and higher order scattering peaks gradually appear. Strong Bragg WAXD peaks, which result from the crystallization of the PEO blocks, also gradually develop upon increasing t_c. From the

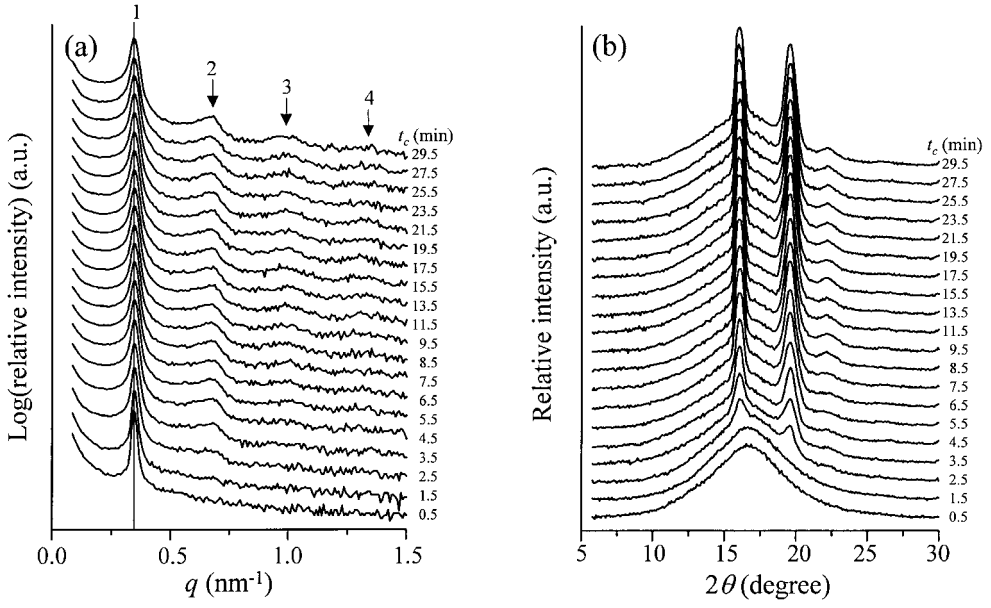

Fig. 6. Sets of 1D SAXS (a) and WAXD (b) patterns for the PEO-*b*-PS isothermally crystallized at 35°C at different times.

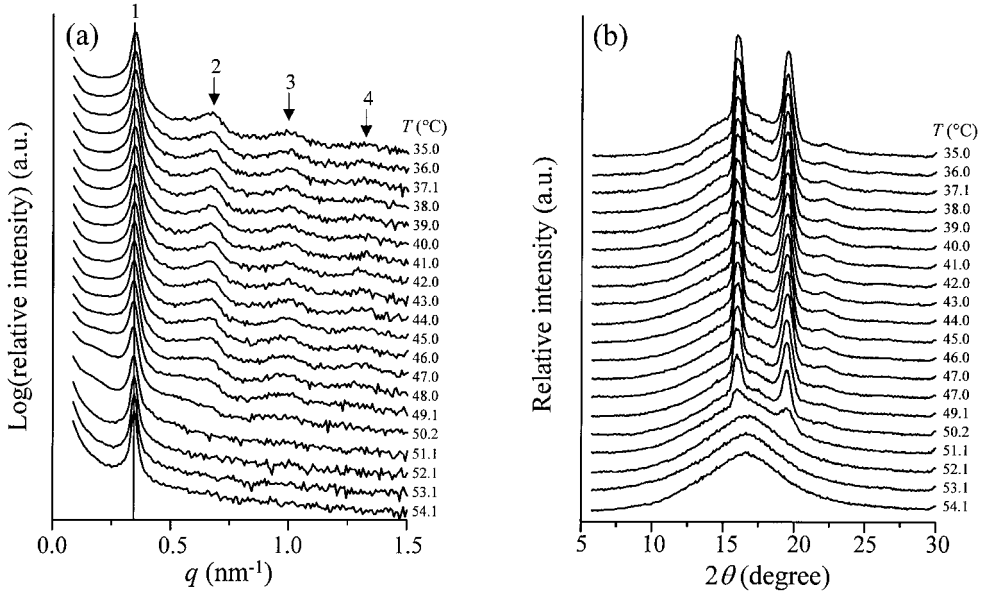

Fig. 7. Sets of 1D SAXS (a) and WAXD (b) patterns for the PEO-*b*-PS recorded during heating to monitor the crystal melting after the sample was completely crystallized at 35°C.

evidence in Fig. 6b, the PEO block crystals possess the same crystal structure as their homopolymer analogs. Since the first-order scattering peak remains at the same q value, and the ordered phase lamellar structure ($q/q^* = 1:2:3:4$) is not changed throughout the crystallization, it can be inferred that the PEO blocks crystallize in a confined space between the PS glassy layers. This is evident since the T_{ODT} of this diblock copolymer is at 160°C, and the T_c is 27°C lower than the T_g^{PS} and 10°C lower than the onset temperature of the T_g^{PS}. Therefore, the confinement, which is formed by rapid vitrification of the PS phase and strong phase segregation of the PEO and PS blocks, effectively constrains the PEO block crystallization. Compared with the crystal lamellar thickness of the PEO homopolymer with the same molecular weight at $T_c = 35°C$ (around 15 nm [52]), the crystal lamellar thickness of the confined PEO crystals (<8.8 nm, because the $\hat{c}$-axis is parallel to $\hat{n}$ at this temperature, see text below) is much thinner. The PEO crystals are thus metastable and constrained within the confined space [53,54].

After crystallization, the first-order scattering peak becomes broader than that in the melt. This is probably due to the existence of a three-phase system formed after crystallization (i.e. PEO crystals, amorphous PEO layers, and amorphous PS layers). The long-range order of the electron density in the two-phase layer structure may be disturbed by this three-phase structure, which would broaden the scattering peaks.

Fig. 7a and b are sets of SAXS and WAXD results for the melting behavior of the PEO-*b*-PS at a heating rate of 1°C/min after the sample was fully crystallized at $T_c = 35$°C. During heating, the SAXS scattering peaks become narrow, while the WAXD Bragg reflections gradually disappear. It is important to note that the positions of the multiple ordered SAXS scattering peaks tend to slightly shift to lower q values as the temperature reaches 45°C, which is the onset temperature of the T_g^{PS}. The solid state characteristics of the PS glassy layers begin weakening at this temperature. The originally constrained PEO crystals tend to thicken along the $\hat{c}$-axis, and as a consequence, expand the overall phase lamellar thickness [53,54].

3.3. Crystal orientation in a confined environment close to room temperature

For this diblock copolymer, the crystal (the $\hat{c}$-axis) orientation in the confined space formed between two PS glassy layers has been observed using combined 2D SAXS and WAXD experiments. The crystal orientation has been observed to change from randomly oriented to perpendicular to $\hat{n}$, then inclined, and finally parallel to the $\hat{n}$, depending upon T_c [55]. Four temperature regions have been observed. At $T_c < -50$°C, the PEO crystals are randomly oriented. At $-50°C \le T_c < -5°C$, the $\hat{c}$-axis of the PEO crystals orients perpendicular to $\hat{n}$. When $-5°C \le T_c < 35°C$, the $\hat{c}$-axis of the PEO crystals is inclined with respect to $\hat{n}$, with the tilt angle increasing with increasing T_c. Finally, for $T_c \ge 35$°C, the $\hat{c}$-axis of the PEO crystals is parallel to $\hat{n}$. In this report, since we are focusing on the crystallization behavior of the PEO-*b*-PS diblock copolymer around room temperature, we only show the 2D SAXS and WAXD results obtained at $T_c \ge 15$°C for shear-aligned samples. Note that these patterns observed along both $\hat{x}$ and $\hat{y}$ directions are identical at all T_cs. In the following discussion, only the diffraction patterns along the $\hat{y}$ direction are displayed to avoid redundancy.

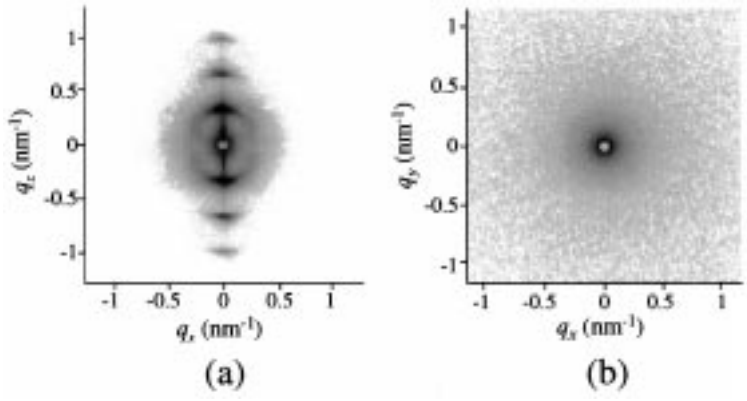

Fig. 8. 2D SAXS patterns through $\hat{y}$ (a) and $\hat{z}$ (b). The intensity in (b) is 10× that in (a).

The lamellar phase morphology for the shear-aligned PEO-*b*-PS sample is studied by 2D SAXS. Fig. 8a shows the SAXS pattern along $\hat{y}$. Up to three scattering orders can be clearly observed. No discernable diffraction in the SAXS pattern through $\hat{z}$ is found in Fig. 8b. Therefore, the phase-separated lamellae are almost perfectly aligned parallel to the shear plane (the $\hat{x}$–$\hat{y}$ plane) based on both the TEM and SAXS results. The 2D WAXD patterns along $\hat{y}$ for the shear-aligned sample isothermally crystallized at 15°C and 40°C are shown in Fig. 9a and b, respectively. The lower angle reflections are (120) reflections, and the higher angle reflections are the overlapped ($\bar{1}$32), (032), ($\bar{2}$12), (112), (124), (204) and (004) reflections. The corresponding azimuthal-scan results for the (120) reflections are given in Fig. 9c and d. One can see four maxims located around 69, 116, 247, and 294° in Fig. 9c. There are also two maxims buried in between the scattering peaks of 69 and 116°, and 247and 294°, respectively, around 90 and 270°. This WAXD pattern can be explained by chain-tilting of the crystals within the confined lamellae [55]. From the azimuthal-scanning result, the tilt-angle with respect to the $\hat{x}$–$\hat{y}$ plane is 66.5° at $T_c = 15$°C. However, there are only two maxims in the azimuthal-scanning result in Fig. 9d, indicating the $\hat{c}$-axis at $T_c = 40$°C is exclusively parallel to $\hat{z}$ ($\hat{n}$). With increasing T_c from 15°C to 40°C, therefore, the crystal orientation changes from inclined to parallel to $\hat{n}$. Detailed analyses show that the transition temperature occurs at $T_c =$ 35°C [55].

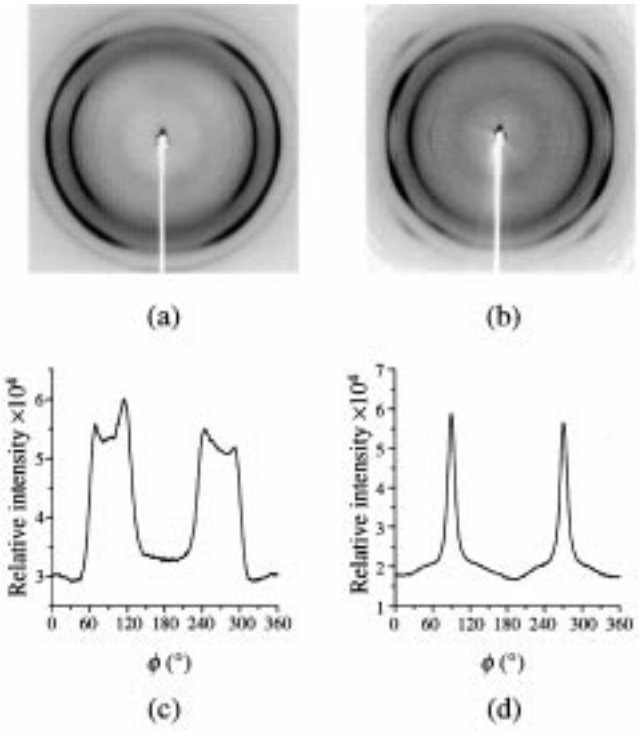

Fig. 9. 2D WAXD patterns along $\hat{y}$ for the shear-aligned sample isothermally crystallized at 15°C (a) and 40°C (b). The corresponding (120) azimuthal-scanning results are shown in (c) and (d) for $T_c = 15$°C and 40°C, respectively.

The 2D WAXD patterns along $\hat{z}$ show isotropic ring reflections for both $T_c = 15$°C and 40°C, indicating the PEO crystals have random distributions along $\hat{z}$. Therefore, the crystal orientations are actually uniaxial around $\hat{n}$ ($\hat{z}$).

3.4. Morphological changes depending upon T_c

If we carefully examine the SAXS results shown in Fig. 10, it is interesting to find that when the sample is crystallized below 35°C the first-order scattering peak tends to shift to larger q values, and the shift amount increases with decreasing T_c. This suggests that the overall phase lamellae slightly shrink along the 1D thickness direction after crystallization. At $T_c = 35$°C, the first-order scattering peak remains at an identical q value as in the melt, and thus, the phase lamellar thickness is constant before and after crystallization. Above $T_c = 35$°C, the first-order scattering peak shifts to smaller q values, and the shift amount increases with increasing T_c. Therefore, the phase lamellae expand along the 1D thickness direction after crystallization. One may speculate that although the phase morphology of the diblock copolymer is frozen by the rapid vitrification of the PS phase, the PEO blocks may slightly

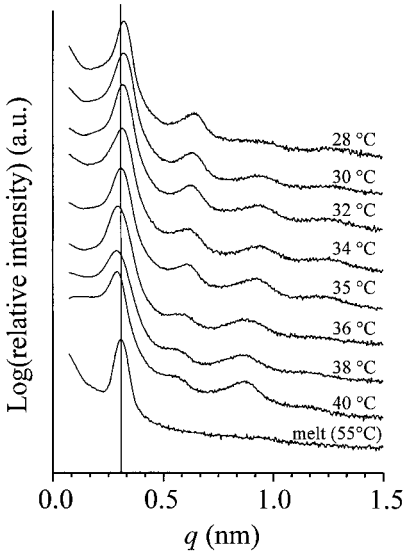

Fig. 10. Set of 1D SAXS data for the PEO-*b*-PS after the samples were crystallized at different temperatures (from $T_c = 28$°C to $T_c = 40$°C).

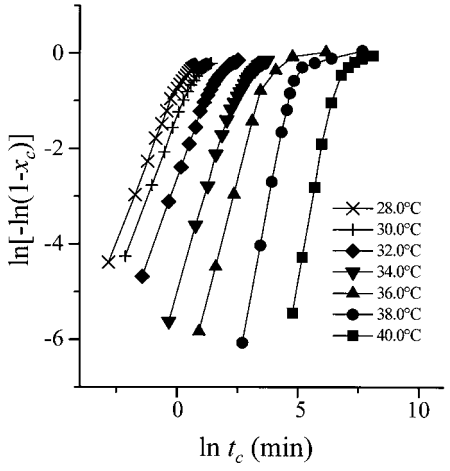

Fig. 11. The Avrami plots of the PEO-*b*-PS crystallized at different temperatures.

manipulate this morphology, when crystallization and/or annealing takes place at temperatures which are less than 10°C lower than the onset temperature of the T_g^{PS}.

These observations can also be related to different crystal orientation transitions with increasing T_c. Note that between $T_c = -5$°C and 35°C, the crystal orientation undergoes a tilt angle change from the perpendicular to the parallel arrangements of the $\hat{c}$-axis with respect to $\hat{n}$ [55]. The temperature where a constant phase lamellar thickness is seen before and after the crystallization is identical to where the crystal orientation has the $\hat{c}$-axis parallel to the $\hat{n}$. Note that the volume of this PEO-*b*-PS diblock copolymer decreases after the crystallization of the PEO blocks [56]. Although the T_g^{PS} is higher than the T_m of the PEO crystals, the change of phase lamellar thickness is 1D and therefore, the sizes of the other two dimensions must change accordingly in order to meet the requirement of the overall volume decrease.

3.5. Overall crystallization kinetics, crystallinity and melting

Fig. 11 shows the overall crystallization kinetics of this PEO-*b*-PS at different T_c studied by DSC, which are plotted using $-\ln[\ln(1 - x_c)]$ vs. $\ln(t_c)$ (x_c is the weight crystallinity, and the results in Fig. 11 will not be much different than volume crystallinity). In the early stage of crystallization, linear relationships appear. From these linear relationships, the Avrami parameters of the intercept [$\ln(K)$] and slope (n) can be obtained as shown in Fig. 12. The $\ln(K)$ includes the geometric factor and linear growth rate terms and can be roughly viewed as a representative of the crystallization rate. In Fig. 12, $\ln(K)$ decreases drastically with increasing T_c, compared with a PEO homopolymer with the same molecular weight. For example, at $T_c = 40.0$°C, $\ln(K)$ is 8.39 for unconfined pure PEO having an $\bar{M}_n$ of 9.0 k [57], while it is -20.5 for the block copolymer. The n value slightly increases at $T_c < 33$°C to between 1.4 and 1.6, implying that the crystal growth of PEO blocks is in a transition from 1D to 2D shapes. This is consistent with the tilting of the c-axis orientation in the PEO crystals. When T_c increases to 35°C, the n value substantially increases to 1.8. This may indicate that the crystallization of PEO blocks at these T_cs become 2D under the confined lamellar environment. Further increasing the T_c leads to another sudden increase of the n value to finally reach 2.9 at $T_c = 39$°C. Compared with the unconfined pure PEO (9.0 k), the n value at 40°C is around 2 in the same T_c region [57]. This may illustrate that the PEO lamellar crystals in the case of pure PEO are not geometrically constrained and therefore, no substantial thickening takes place during the initial stage of the isothermal crystallization. However, the diblock copolymer tends to thicken in the third dimension even in the initial stage, and attempts to overcome the constraint

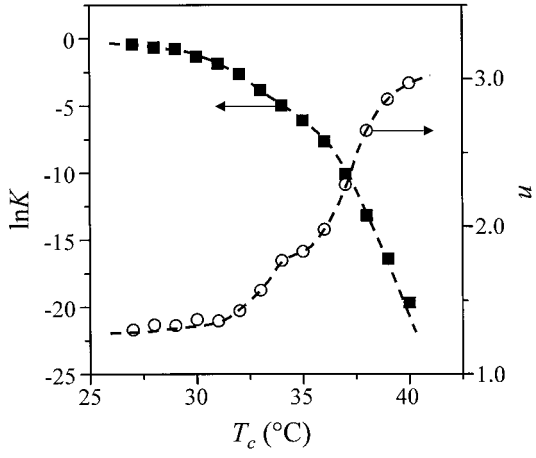

Fig. 12. Changes of the Avrami rate, $\ln(K)$, and the Avrami exponent, n, with respect to the isothermal T_c.

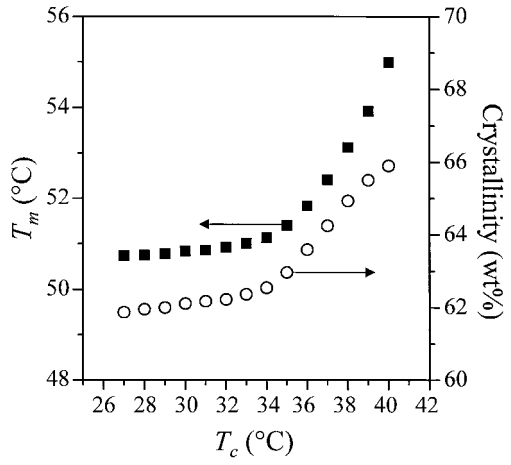

Fig. 13. Changes of the crystallinity and melting temperature with respect to the isothermal T_c.

caused by the PS layers to release the frustration (see Fig. 10). It is also speculated that the change of the growth dimensions and rates in the confined lamellar space may be the cause of the drastic changes in $\ln(K)$.

The T_m and crystallinity changes with respect to T_c are shown in Fig. 13. Both changes possess an onset temperature of 35°C, where the rates of change suddenly increase. This is because the crystallization of the PEO blocks is totally confined when $T_c \leq 35$°C, so the T_m and crystallinity changes are small. When $T_c > 35$°C, the confinement gradually weakens and both quantities increase accordingly. This again corresponds well to the crystal orientation transitions as described in the previous sections. For example, $T_m = 50.8°C$ at $T_c = 30°C$ and $T_m = 51.0°C$ at $T_c = 33°C$. When $T_c = 37°C$, the T_m increases to 53.3°C. Above $T_c > 38$°C, the T_m increases even more rapidly. For example, at $T_c = 40°C$, the T_m reaches 55°C, indicating an increase of the crystal thickness and thus, thermodynamic stability. In other words, as soon as the confinement is weakened, constraints exerted on PEO crystals can be released via crystal thickening.

The crystallinity of the fully crystallized samples is relatively low compared to 93 wt% for the PEO homopolymer having the same $\bar{M}_n$ [52,57]. Again, when $T_c \leq 35$°C, the crystallinity changes little (62% at $T_c = 27$°C, and 62.5% at $T_c = 34$°C). This may reflect the confinement effect on the crystallinity of PEO blocks. However, when $T_c > 35$°C, the crystallinity shows a clear increase. At $T_c = 40$°C, where the confinement effect has been weakened, the crystallinity reaches 66%. We speculate that the lower crystallinity compared to the pure PEO sample may also be caused by the fact that the tethering parts of the PEO chains must be excluded from the crystal lattice.

4. Conclusion

In summary, for the PEO-*b*-PS (8.7–9.2 k) diblock copolymer, the PEO blocks crystallize in a T_c region below 40°C and the PEO crystals melt below 55°C. The breath of the T_g^{PS} transition is 32°C, from 45 to 77°C, and the 50% c_p change during vitrification is at 62°C. The T_{ODT} of this ordered lamellar morphology is experimentally detected at 160°C. The mean-field interaction parameter $\chi_{EO/St}$ is determined to be $-7.05 \times 10^{-3} + 21.3/T$. The PEO blocks thus undergo a crystallization process within a lamellar confined environment between two PS glassy layers. The crystal (the $\hat{c}$-axis) orientation shows transitions from perpendicular to $\hat{n}$ to inclined, to finally parallel to $\hat{n}$ as T_c increases. These results indicate the crystal growth changes from 1D to 2D. Crystallization also leads to a slight change of the phase lamellar thickness. After the PEO block crystallization, the phase lamellar thickness slightly decreases with decreasing T_c when $T_c < 35$°C. Above $T_c = 35$°C, the lamellar thickness slightly increases with increasing T_c, while at $T_c = 35$°C, the thickness remains constant compared with that in the melt. The crystallinity and T_m changes observed after the isothermal crystallization at different T_c also possess an onset temperature of 35°C. This corresponds well to the transition temperature where the crystal (the $\hat{c}$-axis) orientation transfers from inclined to the parallel to $\hat{n}$. Compared with the overall crystallization and melting behavior of a pure PEO with the same $\bar{M}_n$, it can be concluded that the PEO crystals in this diblock copolymer formed in confined lamellar environment are constrained. This constraint can be somewhat released as soon as the confinement is weakened, which is critically determined by T_c when the self-organization and vitrification processes are prevailing processes.

Acknowledgements

This work was supported by the NSF (DMR-9617030). The time-resolved SAXS and WAXD research was carried out in part at the National Synchrotron Light Source in Brookhaven National Laboratory.

References

[1] Bates FS, Fredrickson GH. Annu Rev Phys Chem 1990;41:525.
[2] Matsen MW, Bates FS. Macromolecules 1996;29:1091.
[3] Bates FS, Fredrickson GH. Phys Today 1999;52:32.
[4] Muthukumar M, Ober CK, Thomas EL. Science 1998;277:1225.
[5] Zhu L, Chen Y, Zhang A, Calhoun BH, Chun M, Quirk RP, Cheng SZD, Hsiao BS, Yeh F, Hashimoto T. Phys Rev B 1999;60:10 022.
[6] Yang YW, Tanodekaew S, Mai SM, Booth C, Ryan AJ, Bras W, Viras K. Macromolecules 1995;28:6029.
[7] Ryan AJ, Hamley IW, Bras W, Bates FS. Macromolecules 1995;28:3860.
[8] Nojima S, Kato K, Yamamoto S, Ashida T. Macromolecules 1992;25:2237.
[9] Rangarajan P, Register RA, Fetters LJ, Bras W, Naylor S, Ryan AJ. Macromolecules 1995;28:4932.

[10] Ryan AJ, Fairclough JPA, Hamley IW, Mai SM, Booth C. Macromolecules 1997;30:1723.
[11] Hillmyer MA, Bates FS. Macromol Symp 1997;117:121.
[12] Hamley IW, Fairclough JPA, Bates FS, Ryan AJ. Polymer 1998;39:1429.
[13] Nojima S, Kikuchi N, Rohadi A, Tanimoto S, Sasaki S. Macromolecules 1999;32:3727.
[14] Ishikawa S, Ishizu K, Fukutomi T. Eur Polym J 1992;28:1219.
[15] Quiram DJ, Register RA, Marchand GR, Ryan AJ. Macromolecules 1997;30:8338.
[16] Mai SM, Fairclough JPA, Viras K, Gorry PA, Hamley IW, Ryan AJ, Booth C. Macromolecules 1997;30:8392.
[17] Cohen RE, Cheng PL, Douzinas KC, Kofinas P, Berney CV. Macromolecules 1990;23:324.
[18] Douzinas KC, Cohen RE. Macromolecules 1992;25:5030.
[19] Cohen RE, Bellare A, Drzewinski MA. Macromolecules 1994;27:2321.
[20] Hamley IW, Fairclough JPA, Ryan AJ, Bates FS, Towns-Andrews E. Polymer 1996;37:4425.
[21] Hamley IW, Fairclough JPA, Terrill NJ, Ryan AJ, Lipic PM, Bates FS, Towns-Andrews E. Macromolecules 1996;29:8835.
[22] Sakurai K, MacKnight WJ, Lohse DJ, Schulz DN, Sissano JA. Macromolecules 1993;26:3236.
[23] Khandpur AK, Macosko CW, Bates FS. J Polym Sci, Polym Phys Ed 1995;33:247.
[24] Zhao J, Majumdar B, Schulz MF, Bates FS, Almdal K, Mortensen K, Hajduk DA, Gruner SM. Macromolecules 1996;29:1204.
[25] Liu LZ, Yeh F, Chu B. Macromolecules 1996;29:5336.
[26] Weimann PA, Hajduk DA, Chu C, Chaffin KA, Brodil JC, Bates FS. J Polym Sci, Polym Phys Ed 1999;37:2053.
[27] Quiram DJ, Register RA, Marchand GR. Macromolecules 1997;30:4551.
[28] Quiram DJ, Register RA, Marchand GR, Ryan AJ. Macromolecules 1997;30:8338.
[29] Quiram DJ, Register RA, Marchand GR, Adamson DH. Macromolecules 1998;31:4891.
[30] Lotz B, Kovacs AJ. Kolloid Z Z Polym 1966;209:97.
[31] Lotz B, Kovacs AJ, Bassett GA, Keller A. Kolloid Z Z Polym 1966;209:115.
[32] Kovacs AJ, Lotz B, Keller A. J Macromol Sci Phys B 1969;3(3):385.
[33] Hirata E, Ijitsu T, Hashimoto H, Kawai H. Polymer 1975;16:249.
[34] Séguéla R, Prud'homme J. Polymer 1989;30:1446.
[35] Viras F, Luo YZ, Viras K, Mobbs RH, King TA, Booth C. Makromol Chem 1988;189:459.
[36] Hamley IW, Wallwork ML, Smith DA, Fairclough JPA, Ryan AJ, Mai SM, Yang YM, Booth C. Polymer 1998;39:3321.
[37] Quirk RP, Kim J, Kausch C, Chun MS. Polym Int 1996;39:3.
[38] Morton M, Fetters LJ. Rubber Chem Technol 1975;48:359.
[39] McGowan JC. Polymer 1969;10:841.
[40] Cheng SZD, Wunderlich B. J Polym Sci, Polym Phys Ed 1986;24:577.
[41] Trent JS, Scheinbeim JI, Couchman PR. Macromolecules 1983;16:589.
[42] Fredrickson GH, Helfand E. J Chem Phys 1987;87:697.
[43] Bates FS, Rosedale JH, Fredrickson GH. J Chem Phys 1990;92:6255.
[44] Sakamoto N, Hashimoto T. Macromolecules 1998;31:3815.
[45] Leibler L. Macromolecules 1980;12:1602.
[46] Sakamoto N, Hashimoto T. Macromolecules 1995;28:6825.
[47] Brandup J, Immergut EH, Grulke EA, editors. Polymer handbook 4. New York: Wiley, 1999.
[48] Nagata M, Fukuda T, Inagaki H. Macromolecules 1987;20:2173.
[49] Xu R, Winnik MA, Riess G, Chu B, Croucher MD. Macromolecules 1992;25:644.
[50] Sato T, Katayama K, Suzuki T, Shiomo T. Polymer 1998;39:773.
[51] Wunderlich B. Macromolecular Physics, Crystal structure, morphology and defects, 1. New York: Academic Press, 1973.
[52] Cheng SZD, Barley JS, Zhang A, Habenschuss A, Zschack PR. Macromolecules 1992;25:1453.
[53] Cheng SZD, Keller A. Ann Rev Mater Sci 1998;28:533.
[54] Keller A, Cheng SZD. Polymer 1998;39:4461.
[55] Zhu L, Cheng SZD, Calhoun BH, Ge Q, Quirk RP, Thomas EL, Hsiao BS, Yeh F, Lotz B. J Am Chem Soc 2000;122:5957.
[56] Kovacs AJ, Manson JA. Kolloid Z Z Polym 1966;214:1.
[57] Cheng SZD, Wunderlich B. J Polym Sci, Polym Phys Ed 1986;24:595.